




Compositional order of a symmetric hard-sphere mixture with cross attraction: Role of concentration

Santi Prestipino ¹, Davide Pini ², Dino Costa ¹, Gianpietro Malescio ¹ and Gianmarco Munaò ^{1,*}

¹*Dipartimento di Scienze Matematiche e Informatiche, Scienze Fisiche e Scienze della Terra,
Università degli Studi di Messina, Viale F. Stagno d'Alcontres 31, 98166 Messina, Italy*

²*Dipartimento di Fisica "A. Pontremoli," Università degli Studi di Milano, Via Celoria 16, 20133 Milano, Italy*



(Received 6 May 2025; accepted 18 July 2025; published 13 August 2025)

We investigate a binary mixture of identical hard spheres, interacting through a square-well cross attraction. Recently, we have shown that the equimolar mixture exhibits stripe order (i.e., a regular alternation of layers filled with particles of mostly one species) in both solid and liquid phases [Prestipino *et al.*, *J. Chem. Phys.* **159**, 204902 (2023)]. Here, we extend our study to nonequimolar conditions. Using Monte Carlo simulations, we find a rich self-assembly behavior with several forms of compositional order, depending on the departure from equimolarity and the range of attraction. While stripes are still seen in the solid phase of the 30%/70% mixture, for a larger concentration asymmetry we rather observe fcc ordering of the minority species, provided that the range of attraction is long enough. Due to the possibility to adjust the concentration in the two phases, compositional order is generally richer at solid-vapor coexistence than in the bulk solid: we observe solid droplets with stripes, displaying either square or triangular in-plane order, as well as droplets with bcc structure and honeycomblake order of the minority species in the matrix of the other species. Finally, at sufficiently low temperature the increased concentration of minority particles in the solid droplet makes the cohesive energy at coexistence systematically larger than in the bulk solid.

DOI: [10.1103/y9n7-l7p3](https://doi.org/10.1103/y9n7-l7p3)

I. INTRODUCTION

The spontaneous occurrence of regular patterns in soft-matter systems is a fascinating phenomenon, taking place by molecular self-assembly [1–3]. Through this mechanism, supramolecular structures emerge in a large variety of systems including, among others, colloidal dispersions [4–6], polymeric materials [7,8], amphiphilic systems [9,10], and protein solutions [11]. In this field, computer-aided design offers the unique opportunity to tailor the molecular “building blocks” to a desired target structure [12,13].

Recently, we have shown by Monte Carlo (MC) simulation [14] and density functional theory (DFT) [15] that ordered arrangements spontaneously arise in a model as minimal as a symmetric mixture of hard spheres, with a square-well (SW) cross attraction of tunable width γ . In particular, in the low-temperature solid we have provided evidence for the existence of stripes—patterns where layers rich in one species are regularly alternated with layers rich in the other. For values of γ significantly larger than the particle diameter, stripes also occur in the liquid phase. Interestingly enough, the larger the γ , the better defined and thicker the stripes. The origin of this counterintuitive behavior is the maximization of contacts between unlike particles. In particular, we have shown that under equimolar conditions a striped solid is always more stable than its compositionally disordered counterpart [15]. A remarkable consequence is that stripes are energetically

favored even for γ approaching zero. It goes without saying that the above considerations only apply at low temperature, where the entropic contribution to the free energy is hardly relevant.

Interest in stripe phases stems from their utility in technological applications, including photonic devices and sensors [16], Langmuir and lipid monolayers [17,18], as well as polymer nanocomposites [19]. Yet the microscopic mechanisms underlying the onset of stripes are not completely understood, owing to the wide variety of systems where stripes are observed, ranging from particles interacting via repulsive forces [20–24] to fluids experiencing competing interactions [25–30] and binary mixtures [31–37]. In the first type of system, stripes typically arise when particles repel each other through a two-scale (core-corona) potential. The mechanism at play is different in fluids of particles characterized by a short-range attraction and a longer-range repulsion. The resulting competition between the two components of the potential causes the appearance, at low temperature, of aggregates of various sizes and shapes, including stripes [33,38,39]. The common trait of all such systems is an absolute minimum at nonzero wavevector in the Fourier transform of the interaction potential off the core, favoring spontaneous density modulations. Finally, stripes are also found in binary mixtures where the interaction between like particles is predominantly repulsive and the interspecies force is attractive. In this case, arranging the two species in alternating layers can be energetically advantageous over any other mixing of unlike particles.

The stripe phases discussed in Refs. [14,15] were observed under equimolar conditions, for a quite extended range of

*Contact author: gianmarco.munao@unime.it

densities, temperatures, and SW widths. On the other hand, we know from previous studies on similar systems that changing the relative concentration of the species substantially affects the size and shape of aggregates in the mixture, as well as the very existence of stripes [31,35]. The leading role of concentration has already been recognized both for spherical [40,41] and nonspherical particles [42,43]. Here, we carry out a similar study for our model mixture, by systematically investigating through MC simulations the existence of complex motifs away from equimolarity; the role played by the range of SW attraction is examined as well.

The outline of the paper is as follows. In Sec. II we introduce the model and describe the method used for its investigation. Simulation results are presented and discussed in Secs. III and IV, where moderate and large compositional asymmetries are respectively addressed. The final section, Sec. V, is devoted to conclusions and outlook.

II. MODEL AND SIMULATION METHOD

Our mixture is composed of two species of hard spheres (labeled A and B) with equal diameter σ , which mutually interact through a SW potential u_{AB} of range $(1 + \gamma)\sigma$:

$$u_{AB}(r) = \begin{cases} +\infty & \text{if } r < \sigma \\ -\varepsilon & \text{if } \sigma \leq r < \sigma + \gamma\sigma, \\ 0 & \text{otherwise} \end{cases} \quad (1)$$

r being the interparticle distance. From now on, all quantities are expressed in units of σ and ε .

At variance with our previous studies [14,15], here we consider concentrations $\chi = N_B/N$ departing from equimolarity (i.e., $\chi \neq 0.5$), N and N_B being the total number of particles and the number of B particles, respectively. We denote by ρ the total number density in a volume V , i.e., $\rho = N/V$. In particular, by fixing $N = 2048$ we examine two cases, $\chi = 0.3$ and $\chi = 0.1$ (hence, the minority species is B). For each value of χ , we consider both $\gamma = 1$ and $\gamma = 0.5$.

We investigate the structure and energy of the mixture by canonical MC simulations of samples enclosed in a cubic box with periodic boundary conditions. In the high-temperature (supercritical) regime, we typically perform 10^6 MC cycles to equilibrate the system and the same number of cycles to compute equilibrium data. In the subcritical regime, we employ up to 5×10^7 MC cycles to equilibrate the system, followed by 5×10^6 cycles in the production stage. To speed up relaxation to equilibrium, even near the close-packing density $\sqrt{2}$, we implement swapping moves to interchange the identity of two randomly chosen unlike particles.

Liquid-vapor equilibria are determined by Gibbs-ensemble MC (GEMC) simulations—see, e.g., Ref. [44]—using two initially identical simulation boxes. We typically carry out runs of 10^6 cycles, one cycle corresponding to (an average of) N displacements plus one volume exchange plus a few hundred particle exchanges plus a few dozen swapping moves.

The amount of local crystalline order is quantified by the Steinhardt orientational order parameters (OOPs) q_4 and q_6 [45–47]. Both quantities are nearly zero for a particle in a liquidlike environment, whereas they are significantly nonzero for a solidlike particle. The values of q_4 and q_6 averaged over all particles (\bar{q}_4 and \bar{q}_6) can discriminate a liquidlike from a

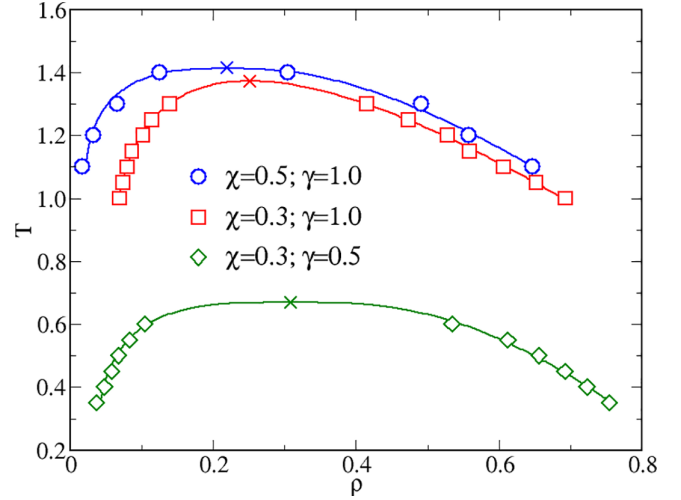


FIG. 1. GEMC liquid-vapor coexistence points (symbols) for various χ and γ , in the legend. Data at equimolarity taken from Ref. [14]. Lines are best fits based on the law of rectilinear diameters and the scaling law for the density difference; crosses indicate the corresponding critical points.

solidlike droplet in vapor. When combined with visual inspection of selected system configurations, the density evolution of \bar{q}_4 and \bar{q}_6 provides a useful mean to sketch the phase diagram. Finally, the structure of the mixture is also probed by correlation functions (namely, radial distribution functions and structure factors), as well as by the probability distribution of the number of bonds.

III. MODERATE COMPOSITIONAL ASYMMETRY

Liquid-vapor coexistence curves for $\chi = 0.3$ are reported in Fig. 1 for two values of γ , along with the coexistence curve for $\chi = 0.5$ and $\gamma = 1$, taken from Ref. [14]. At each temperature, GEMC simulations were started with $\rho = 0.25$ in both boxes. We remark that, at variance with the equimolar mixture, for $\chi \neq 0.5$ the densities of the coexisting phases depend on the total density chosen. This we checked explicitly in the case $\chi = 0.3$ and $\gamma = 0.5$ by performing simulations (for $T = 0.5$) at three densities, namely, 0.15, 0.25, and 0.35: as ρ increases, the coexistence curve shrinks, albeit slightly. We reckon that, for the χ and γ considered here, the value $\rho = 0.25$ is sufficiently near the critical density to allow for an estimate of the critical points by extrapolation of the GEMC data. To ascertain this point, we use the mean-field theory (MFT) phase diagram [48] as a test bed, by implementing on it the same procedure used on the GEMC results. Specifically, we considered the MFT liquid-vapor coexistence curve in the ρ - T plane for $\chi = 0.3$, $\gamma = 0.5$, and $\rho = 0.25$ in a temperature range similar to that of the simulation data, and fitted it to the law of rectilinear diameters and the scaling law for the density difference between liquid and vapor. The resulting estimates for the critical density and temperature ρ_c , T_c were found to differ from the actual MFT values $\rho_c = 0.276$, $T_c = 0.606$ by 3% and 0.3%, respectively.

The MFT critical density is actually independent of γ , whereas this is not the case for the simulation results. For $\chi = 0.3$ and $\gamma = 0.5$, extrapolation of GEMC data to the

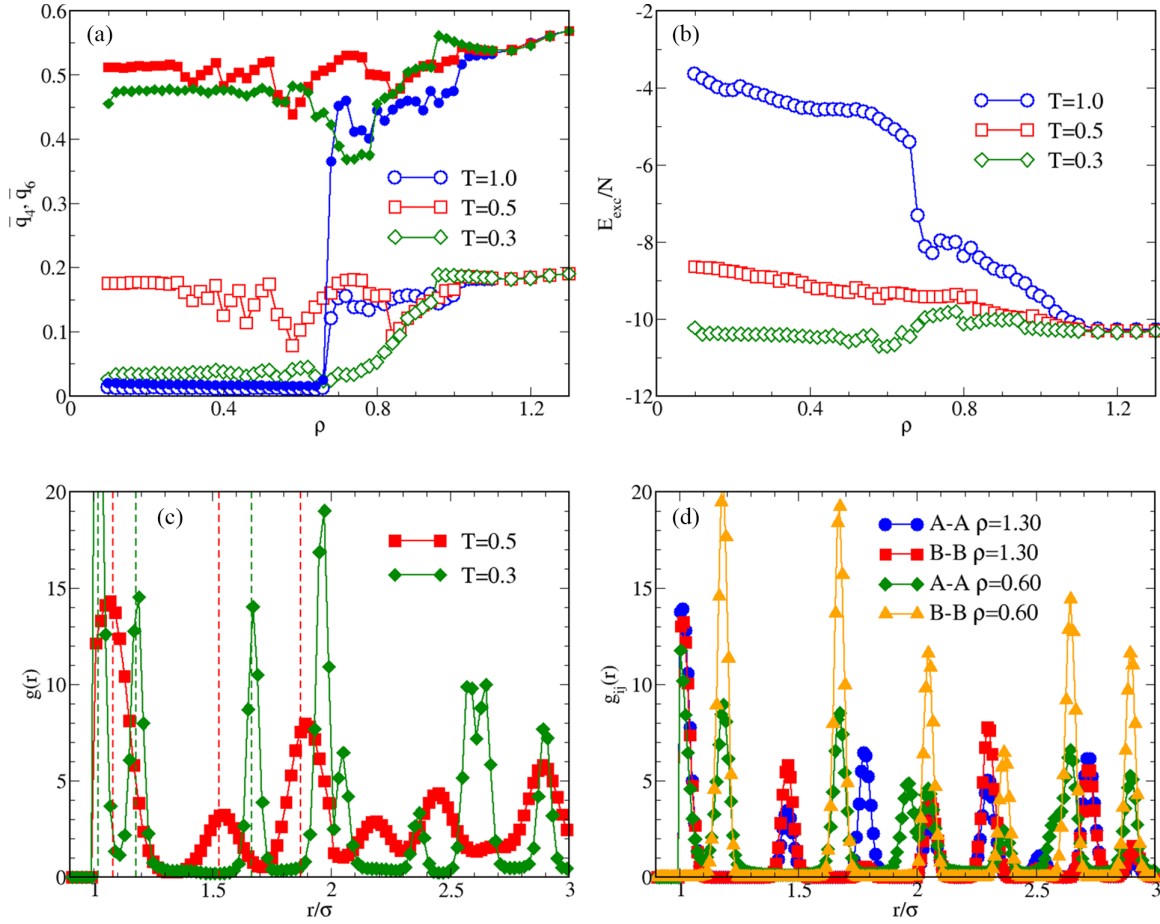


FIG. 2. Mixture for $\chi = 0.3$ and $\gamma = 1$. (a) orientational order parameters \bar{q}_4 (empty symbols) and \bar{q}_6 (full symbols). (b) excess energy per particle. (c) total radial distribution function for $\rho = 0.3$ and two temperatures (in the legend). We recall that the ratio of second- (third-) to first-neighbor distance is $\sqrt{2}$ ($\sqrt{3}$) for fcc (red dashed lines), while being $2/\sqrt{3}$ ($2\sqrt{2}/3$) for bcc (green dashed lines). (d) comparison between A-A and B-B radial distribution functions at $T = 0.3$, for $\rho = 1.3$ and 0.6 .

critical region gives $\rho_c = 0.308$, $T_c = 0.669$. Since the estimated ρ_c is farther from the value $\rho = 0.25$ used in the simulations than the MFT result, the error with respect to the actual critical point is probably slightly larger, but should not exceed a few percent. On the other hand, for $\chi = 0.3$ and $\gamma = 1$ the same procedure gives $\rho_c = 0.252$, $T_c = 1.373$, the estimated ρ_c being now very close to $\rho = 0.25$. In this case, we expect the error to be smaller than that obtained in MFT.

On all curves in Fig. 1, the lowest- T data correspond to the smallest temperature at which liquid-vapor equilibrium could be established by GEMC; hence this T value can be taken as a rough estimate of the temperature of the solid-liquid-vapor triple point, which would plausibly fall immediately below. We see in the figure that, moving away from equimolarity, both the critical point and the triple point of the mixture are shifted down in temperature, the more so the lower the γ . Moreover, it emerges from our data that the location of the liquid-vapor region in the phase diagram is more affected by the SW width than by concentration.

Next, we explore by MC simulations the behavior of the mixture for $\chi = 0.3$. We examine only a few isotherms, namely, $T = 1, 0.5$, and 0.3 , while thermalization at lower temperatures proved difficult. Starting from a substitutionally disordered fcc crystal at $\rho = 1.4$, we reduce the density in

0.02 steps, until reaching $\rho = 0.1$. By performing our runs in a sequence we hopefully minimize the error associated with a slow relaxation to equilibrium.

To qualify the global structure as solid or fluid we compute \bar{q}_4 and \bar{q}_6 . We first consider $\gamma = 1$ [see Fig. 2(a)]. For $T = 1$, \bar{q}_4 and \bar{q}_6 are significantly nonzero—and the mixture is crystalline—down to $\rho \simeq 1.0$. Upon reducing the density further, the OOPs steadily decrease, suggesting that we are crossing the solid-liquid region. The abrupt fall observed at $\rho \simeq 0.70$ indicates that the solid has eventually undergone complete melting. All phase boundaries located in this way are clearly only approximate, since being affected by hysteresis. For $T = 0.5$ and $T = 0.3$ the scenario is different. Now, \bar{q}_4 and \bar{q}_6 remain nonzero down to $\rho = 0.1$, pointing to solid-vapor coexistence below $\rho \simeq 1.0$. We have verified that, across this range of densities, the shape of the solid droplet changes according to the same universal pathway identified for one-component fluids [49–51]. In conclusion, the triple-point temperature falls between $T = 0.5$ and 1 , which is consistent with Fig. 1.

A curious feature seen in Fig. 2(a) is the nonmonotonic temperature behavior of the OOPs. This can be explained by the different structure of the solid droplet at $T = 0.5$ and $T = 0.3$. In fact, we have computed the total radial

distribution function (i.e., the one blind to the particle species) at $\rho = 0.3$ [see Fig. 2(c)] and found that the location of the first three peaks is rather different at the two temperatures, and indicative of the existence of local fcc (bcc) order at $T = 0.5$ (0.3). The typical OOP values for these two structures [46] are consistent with the values seen in Fig. 2(a). We deem it remarkable that a solid droplet made of hard spheres with a SW interspecies attraction exhibits a bcc structure. This can only be ensured by an adequate compositional order (see more below).

The structural difference between the droplet and the bulk solid also emerges from the shape of the radial distribution functions $g_{AA}(r)$ and $g_{BB}(r)$ for $T = 0.3$, plotted in Fig. 2(d) for two densities. The location of peaks indicates that even the species-resolved structure is fcc in the bulk solid, while it is bcc-like in coexistence.

The excess energy per particle (E_{exc}/N) for $\gamma = 1$ is reported in Fig. 2(b). Its value is ≈ -10.5 for all densities above ≈ 1.1 and all temperatures. For $T = 1$, a gradual expansion of the system causes the energy to increase monotonically, until, at $\rho \approx 0.7$, an upward jump occurs in coincidence with the abrupt fall of \bar{q}_4 and \bar{q}_6 . Such a jump is absent for $T = 0.5$ and 0.3, since at these temperatures solid and vapor coexist.

The excess energy for $T = 0.3$ has an intriguing feature: upon reducing ρ , the energy first increases and then, at $\rho \simeq 1.0$, starts decreasing, remaining lower than in the bulk solid in a wide range of moderate densities. As we are going to show in the following, this behavior reflects a difference in composition between the solid droplet and the bulk solid.

To characterize in detail the composition of the mixture, we have carried out a detailed visual inspection of microscopic configurations, which for $\gamma = 1$ is summarized in Fig. 3. Therein we see that, for $T = 1$ [Fig. 3(a)], the fcc solid for $\rho = 1.2$ is a striped solid, i.e., made of alternating layers filled with particles of the same species. In particular, B layers consist of single planes, whereas A layers are made of two planes; particles of both species display in-plane square order (notice that a sample with $N = 2048$ particles is frustrated, since one more plane of particles would be needed in the box to fit the natural system periodicity at this density). This structure is different from what is observed under equimolar conditions [14,15], where A and B layers have the same number of planes (see, e.g., Fig. 3 of Ref. [14]). Also notice that $\chi = 0.3$ slightly deviates from the ideal 1/3 concentration of the structure just described, meaning that the structure of the sample contains additional spurious defects. For $T = 0.5$ and $\rho = 0.8$ [Fig. 3(b)], the solid coexists with an extremely dilute vapor, as typically occurs below $\rho \simeq 1.0$. Under these conditions, the solid droplet (in this case a slab) shows the same A and B alternation of the bulk solid for $T = 1$. However, upon further lowering T to 0.3, a change in compositional order—hinted at by the behaviors of the OOPs and E_{exc} —occurs below $\rho \approx 0.7$ [Fig. 3(c)]: away from the surface, we see a diffuse honeycomblike arrangement of minority particles, which admittedly is responsible for the bcc ordering of the solid droplet mentioned before.

Now turning to $\gamma = 0.5$ [Fig. 4(a)], when $T = 0.5$ we see that the OOPs vanish below $\rho \approx 0.8$. Therefore, at variance with $\gamma = 1$ the system is still above its triple point for $T =$

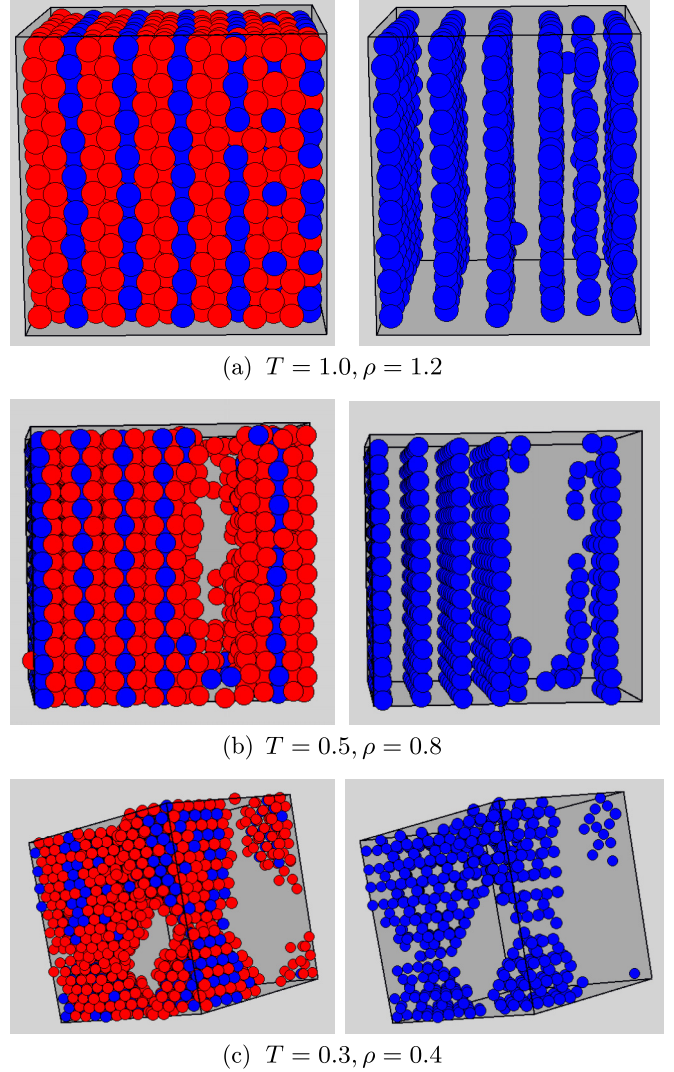


FIG. 3. A few snapshots of the mixture for $\chi = 0.3$, $\gamma = 1$ and different thermodynamic conditions: $T = 1.0$, $\rho = 1.2$ (a); $T = 0.5$, $\rho = 0.8$ (b); $T = 0.3$, $\rho = 0.4$ (c). A and B particles are colored in red and blue, respectively. In the right panels, A particles have been removed to make it evident that B particles form ordered structures.

0.5, again in agreement with the data in Fig. 1. The scenario changes when the temperature drops to 0.3: now, \bar{q}_4 and \bar{q}_6 are significantly nonzero also at low density, signaling that the triple-point temperature has been crossed. The behavior of the excess energy for $\gamma = 0.5$ [Fig. 4(b)] is qualitatively similar to $\gamma = 1$.

For $\chi = 0.5$ and $\gamma = 0.5$, we know (from Fig. 11 of Ref. [15]) that the stripes in the solid consist of single planes for both species, with triangular ordering of particles in the planes. Also for $\chi = 0.3$ stripes are present in the bulk solid, but in the planes hosting the B particles one sublattice out of three is actually occupied by A particles; such an arrangement would imply a concentration of 1/3, which reduces to the actual 0.3 in the presence of defects. We underline that this stripe order only exists in the high-density regime, regardless of T , becoming poorly defined already for $\rho \approx 1.2$, even though the

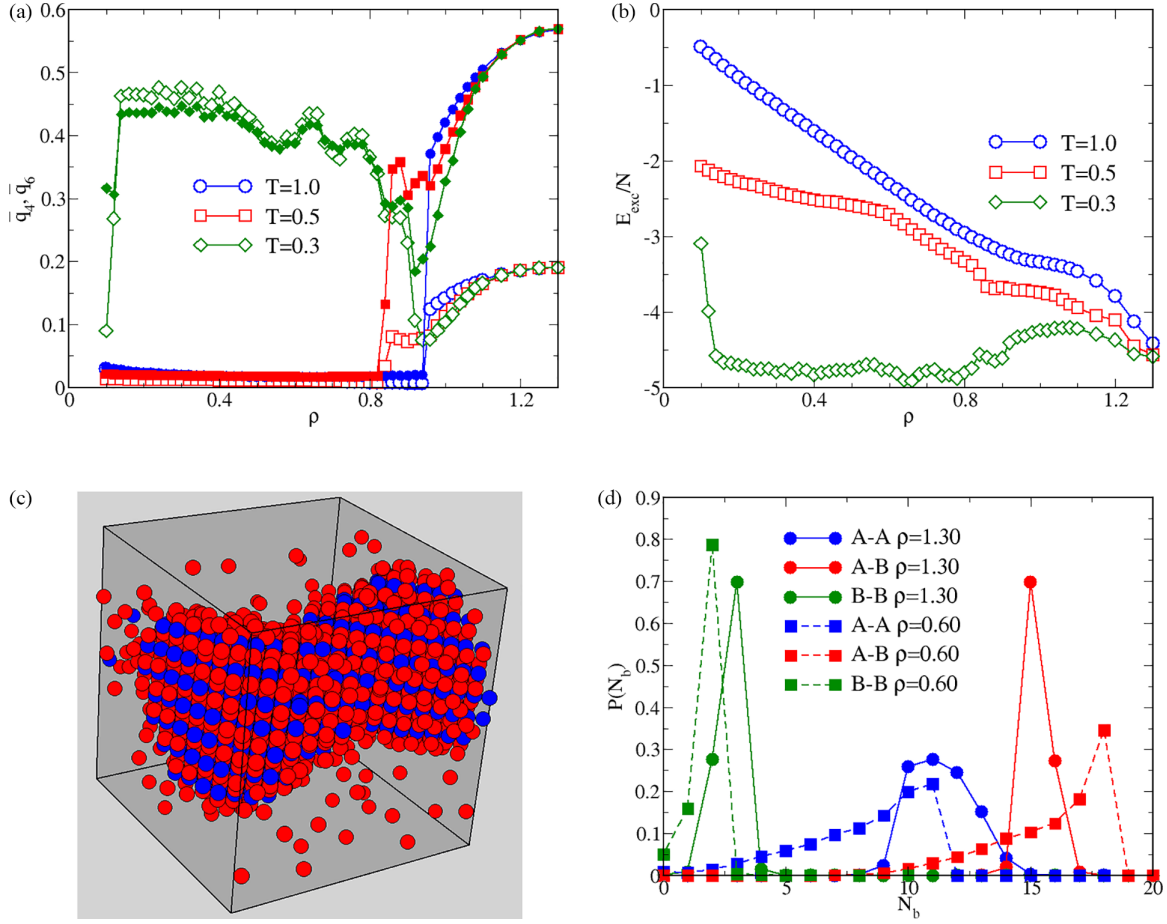


FIG. 4. Mixture for $\chi = 0.3$ and $\gamma = 0.5$. (a) orientational order parameters \bar{q}_4 (empty symbols) and \bar{q}_6 (full symbols). (b) excess energy per particle. (c) snapshot of the mixture for $T = 0.3$ and $\rho = 0.3$. (d) probability distribution of bonds at $T = 0.3$, for $\rho = 1.3$ and $\rho = 0.6$.

solid exists as a stable phase down to $\rho \approx 1$. For densities lower than 1, some hints of stripe order are also found in the dense liquid for $T = 0.5$, at least above $\rho \approx 0.8$. For $T = 0.3$, the solid coexists with vapor in the whole interval $0.1 \lesssim \rho \lesssim 0.9$ and again a different compositional order arises. Looking, e.g., at the cylindrical droplet shown in panel (c) of Fig. 4, B particles exhibit square (rather than triangular) order, which is made possible by a concentration of B particles in the core of the droplet larger than 0.3.

To summarize, it is clear that changes in compositional order are essentially driven, at not too high temperatures, by the associated energy gain. In turn, it is precisely the ability of the two-phase system to self-organize differently from the bulk solid that can make the excess energy of the droplet lower. This is transparent in the behavior of the probability distribution of bond number, $P(N_b)$, reported for each type of bond in Fig. 4(d), for $\gamma = 0.5$, $T = 0.3$, and two densities. Two particles are considered “bonded” if their distance falls within the range of SW attraction. Looking at the figure, the distributions of A-A and B-B bonds are sharply peaked in the bulk solid and less so in coexistence, as expected. Much more interesting is the probability distribution of the number of A-B bonds: while in coexistence ($\rho = 0.6$) each B particle is typically bonded to 18 A particles, in the bulk solid ($\rho = 1.3$) the number of bonds per B particle drops to 15. This demonstrates how a different compositional order

in the solid droplet can make the number of A-B bonds larger than in the bulk solid and, consequently, how a more favorable energetic condition is found in the former case. The same behavior is observed, with different nuances, for all combinations of χ and γ investigated in this paper; thus it likely represents a general feature of the nonequimolar mixture.

IV. STRONG COMPOSITIONAL ASYMMETRY

In the more asymmetric $\chi = 0.1$ case, only one particle out of ten belongs to species B. Yet, we will see that the behavior of the mixture is radically different from pure hard spheres. Choosing $\gamma = 1$ first, the OOPs are shown in panel (a) of Fig. 5, and the excess energy per particle in panel (b). The overall behavior of \bar{q}_4 and \bar{q}_6 is similar to $\chi = 0.3$, in spite of quite higher cohesive energies. As testified by the OOP values at low density, the triple-point temperature is between $T = 0.5$ and 1. For $T = 0.3$ we recover the same behavior observed for $\chi = 0.3$, i.e., an absolute energy minimum located in the solid-vapor region.

As far as composition is concerned, we see in the snapshots of the mixture for $\gamma = 1$ and $T = 1$ that in the high-density regime [Fig. 6(a)] the compositional order is different from $\chi = 0.3$ and again novel: B particles now form a fcc crystal on their own, with a first-neighbor distance close to 2σ . This

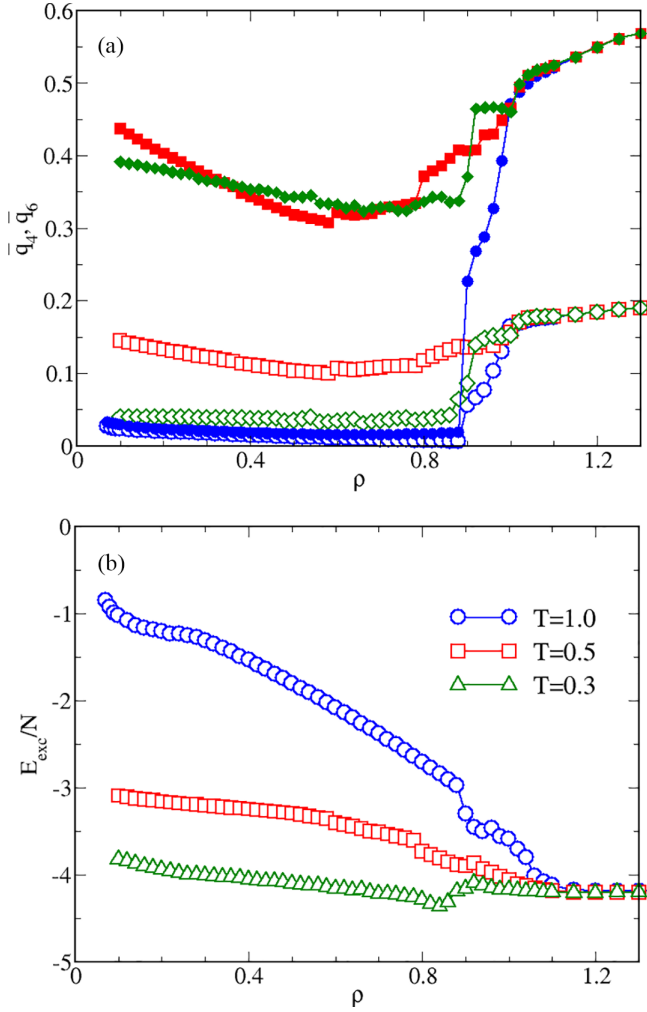


FIG. 5. Mixture for $\chi = 0.1$ and $\gamma = 1$. (a) orientational order parameters \bar{q}_4 (empty symbols) and \bar{q}_6 (full symbols). (b) excess energy per particle. Temperatures are in the legend of panel (b).

would amount to $\chi = 1/8$, implying that some of the fcc sites pertaining to B particles are actually occupied by A particles. This peculiar order vanishes when reducing the density below 1.0, where a substitutionally disordered solid is found instead [Fig. 6(b)]. Finally, at $\rho \simeq 0.6$ the system enters the liquid-vapor region.

Below the triple-point temperature, the bulk solid extends down to $\rho \approx 1.1$; for slightly lower densities, solid-vapor coexistence occurs. Under these conditions, the solid droplet has the same compositional order observed in bulk. However, below $\rho \approx 0.8$ the compositional order changes, becoming stripe order: in the solid droplet, planes occupied by B particles are alternated with two-plane layers filled with A particles. In particular, for $T = 0.5$ B particles show in-plane square order [Fig. 6(c)], whereas for $T = 0.3$ the ordering of B particles is similar to that in the bulk solid for $\chi = 0.3$ and $\gamma = 0.5$ (namely, in the planes filled with B particles, one triangular sublattice out of three is occupied by the A species).

All these peculiarities find a rationale in the strong concentration unbalance between the species. In order to minimize energy at low temperature, the vapor phase is remarkably

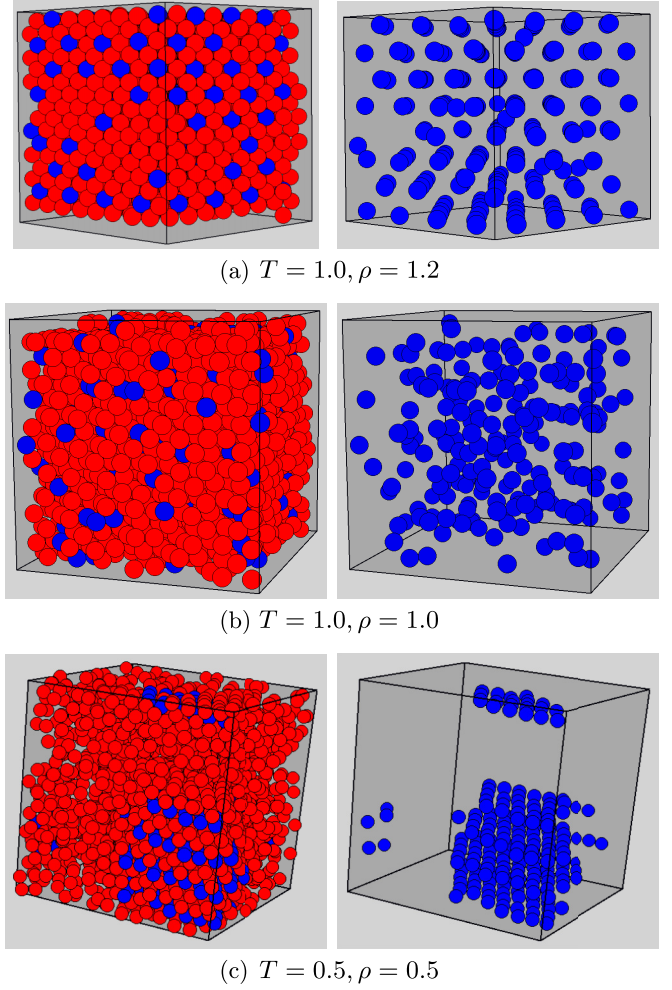


FIG. 6. A few snapshots of the mixture for $\chi = 0.1$, $\gamma = 1$ and different thermodynamic conditions: $T = 1.0$, $\rho = 1.2$ (a); $T = 1.0$, $\rho = 1.0$ (b); $T = 0.5$, $\rho = 0.5$ (c). In the right panels, A particles have been removed to show the arrangement of B particles.

dense and practically devoid of B particles—for example, in the configuration reported in Fig. 6(c), the vapor density is about 0.45, which is quite high for a vapor phase, but, at the same time, too low for surmising that the vapor would actually be a solid. The remaining A particles are bound to B particles in the solid droplet, where the effective χ is substantially higher than the nominal 0.1, thus allowing for the possibility of stripe order.

Finally, we analyze the mixture for $\chi = 0.1$ and $\gamma = 0.5$. The OOPs are shown in panel (a) of Fig. 7, and the excess energy per particle in panel (b). The triple-point temperature is between 0.2 (where \bar{q}_4 and \bar{q}_6 are small but definitely nonzero in a range of moderate densities) and 0.3 (where \bar{q}_4 and \bar{q}_6 vanish for all densities lower than 1.0). Interestingly, for $T = 0.2$ the OOPs are close to zero for $\rho < 0.3$; moreover, the excess energy shows a broad minimum for moderate densities, lower than the energy of the bulk solid. With an attraction of very short range between unlike particles, the B particles would be too few to support compositional order of any kind. Indeed, the solid phase is a substitutionally disordered fcc crystal, regardless of the temperature. At $T = 0.3$ or higher,

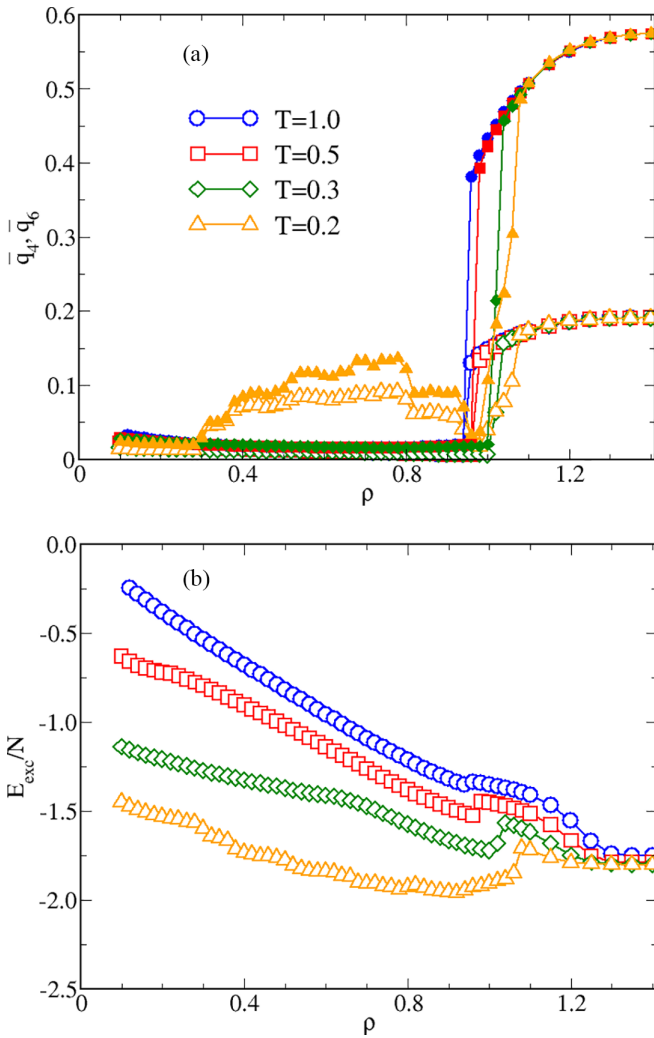


FIG. 7. Mixture for $\chi = 0.1$ and $\gamma = 0.5$ (temperatures in the legend). (a) orientational order parameters \bar{q}_4 (empty symbols) and \bar{q}_6 (full symbols). (b) excess energy per particle. Temperatures are in the legend of panel (a).

the solid melts into liquid for $\rho \approx 1$; for still lower densities the mixture lies in the liquid-vapor region, as suggested by the behavior of the static structure factor. In Fig. 8, the A-A structure factor is plotted as a function of the wavevector for several densities at $T = 0.3$. As ρ is lowered, the increasing trend of $S_{AA}(k)$ for vanishing wavevectors points towards the development of density fluctuations on progressively longer interparticle distances, as typically occurs when approaching the liquid-vapor coexistence region.

A more interesting behavior shows up at $T = 0.2$, where the mixture manages to reduce its energy below the value typical of the bulk solid by gathering B particles in a small region of the box—a solution that clearly requires two-phase coexistence. We remark that also at $T = 0.2$ no compositional order occurs in the bulk solid, which begins to melt around $\rho = 1.0$. Starting with $\rho \approx 0.8$, the solid droplet develops a form of compositional order where B particles are arranged in a regular structure, close to fcc (see Fig. 9).

Further details on the arrangement of particles for $T = 0.2$ can be gained by computing the radial distribution func-

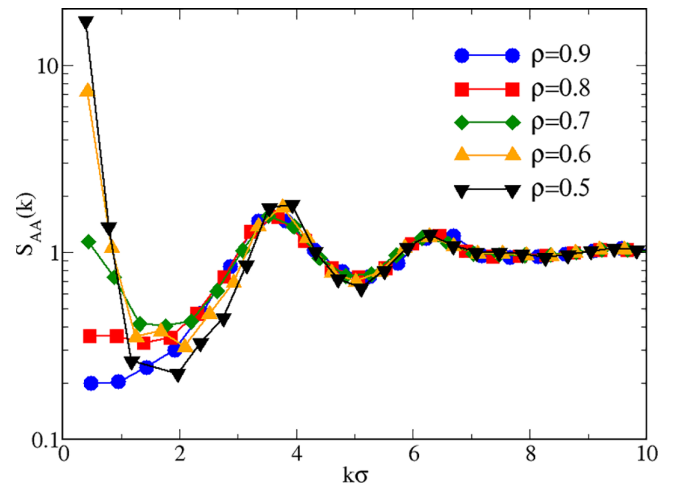


FIG. 8. Structure factor $S_{AA}(k)$ for $\chi = 0.1$, $\gamma = 0.5$, and $T = 0.3$. Densities ρ are in the legend.

tions $g_{AA}(r)$ and $g_{BB}(r)$ for $\rho = 1.3$ (bulk solid) and $\rho = 0.8$ (solid-vapor coexistence); see Fig. 10(a). As expected, for $\rho = 1.3$ the shape of both functions is consistent with solidlike behavior, with narrow peaks at lattice distances. Conversely, for $\rho = 0.8$, A particles are not in perfect registry and their environment is distorted enough to appear liquidlike, whereas B particles keep locally a crystalline arrangement. Apparently, this arrangement is the only possibility for B particles to make bonds with a higher number of A particles than in the bulk solid. This is demonstrated in Fig. 10(b), where the probability distributions of the number of A-A, B-B, and A-B bonds are plotted. It clearly emerges that, for $\rho = 0.8$, each B particle is typically bonded to 19 or 20 A particles, i.e., more than in the bulk solid where the number of bonds is exactly 18. Also notable is the strong density dependence of the A-A bond distribution, which at $\rho = 0.8$ is dominated by vapor. Finally, when the density becomes too low, the size of the droplet decreases considerably, until it melts completely. However, this should not be interpreted as the reentrance of liquid-vapor equilibrium but rather as a size effect due to the smallness of the simulation sample.

While in principle novel structures and compositions can emerge at concentrations not considered here, we believe that a critical comparison of our three cases (including equimolar conditions [14,15]) already reveals a few general trends in

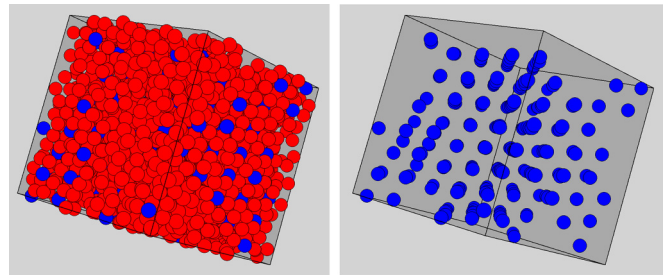


FIG. 9. Left: snapshot of the mixture for $\chi = 0.1$, $\gamma = 0.5$, $T = 0.2$, and $\rho = 0.78$. In the right panel, A particles have been removed to highlight the position of B particles.

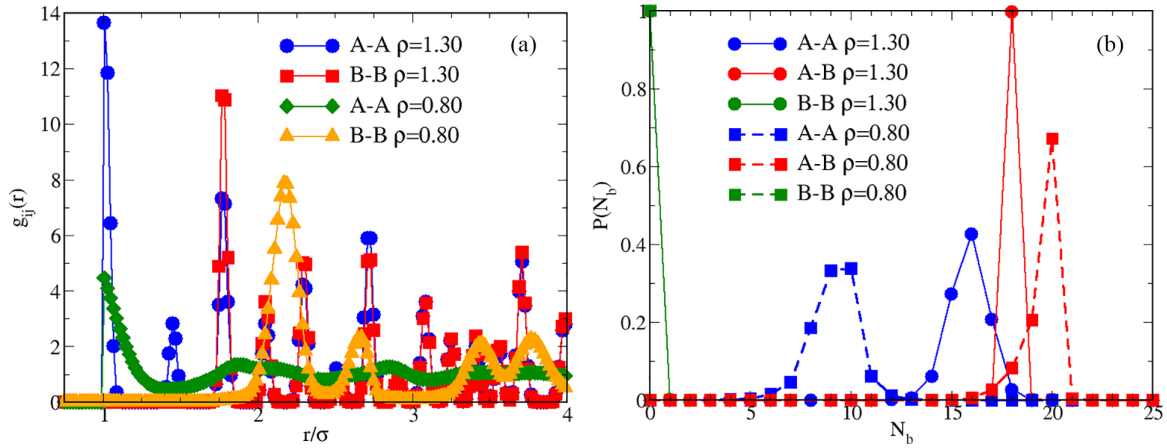


FIG. 10. Mixture for $\chi = 0.1$ and $\gamma = 0.5$ at $T = 0.2$, for $\rho = 1.3$ and 0.8 . (a) comparison between A-A and B-B radial distribution functions. (b) Probability distribution of bonds.

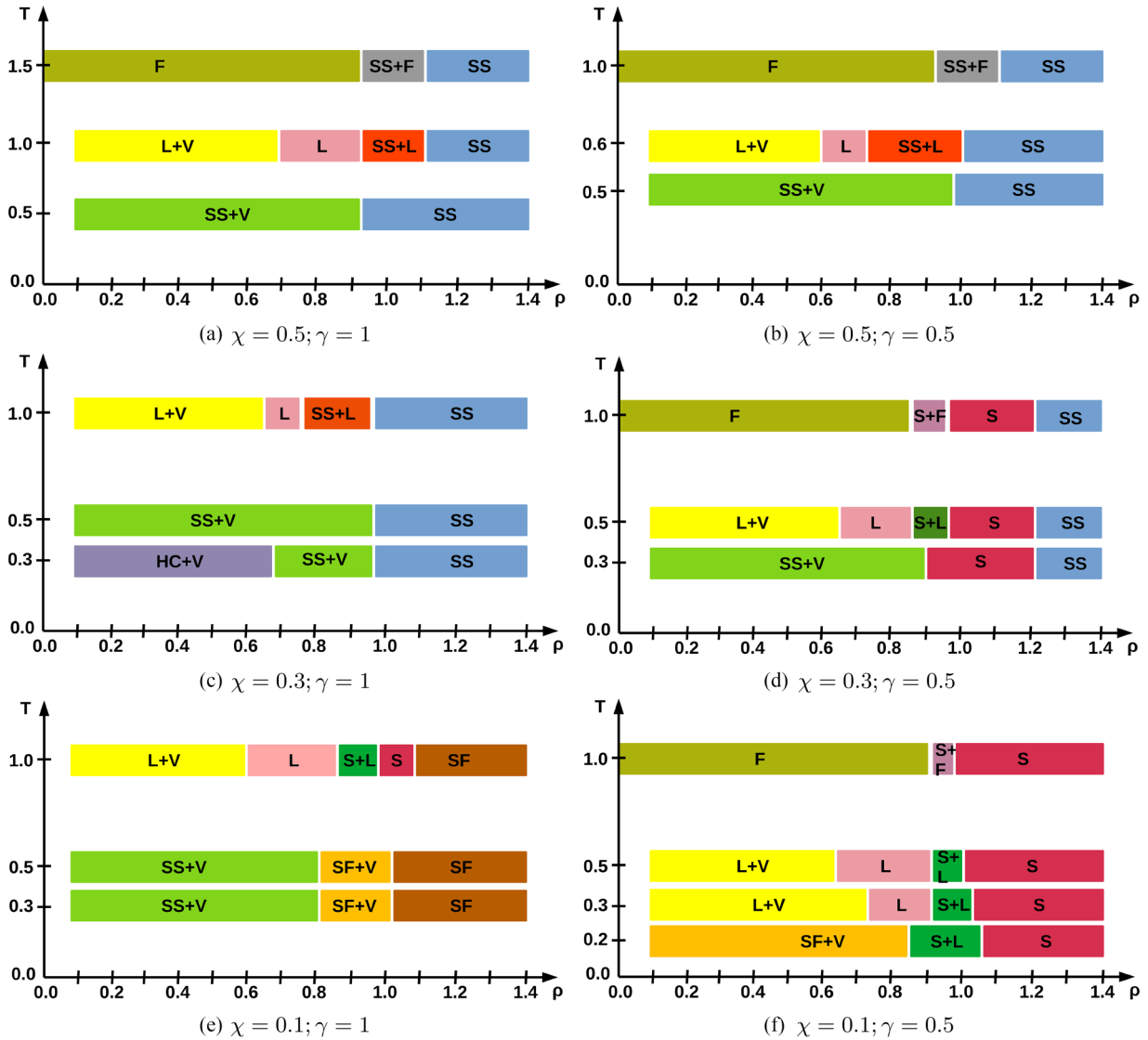


FIG. 11. Schematic phase diagrams of the mixture in the density-temperature plane for all the combinations of χ and γ investigated in this paper [panels c–f]. In panels (a), (b), the diagrams corresponding to equimolar conditions are reported for comparison [14,15]. The phase boundaries are only approximate. Abbreviations are the following: V (vapor), L (liquid), SS (striped solid), HC (honeycomb structure of B particles), F (fluid), S (substitutionally disordered fcc solid), and SF (fcc solid with fcc ordering of B particles).

the combined effects of χ and γ on the phase behavior of the mixture. For such an aim, a schematic summary of all phase behaviors is presented in Fig. 11. Upon increasing the departure from equimolarity, it emerges that stripes, which are systematically observed in the bulk solid for $\chi = 0.5$ and 0.3 , only survive in the solid-vapor region for $\chi = 0.1$ and $\gamma = 1$, while being altogether absent for $\gamma = 0.5$. Moreover, a difference in compositional order between the bulk solid and the solid droplet is only seen under nonequimolar conditions. Finally, while the value of γ does not significantly affect the phase behavior for $\chi = 0.5$, the opposite is true at the other concentrations.

V. CONCLUSIONS

We have investigated by Monte Carlo simulations the nature of compositional order in a mixture of two identical hard-sphere species, with the cross interaction modeled by a square-well (SW) potential. This system represents the simplest conceivable model of binary mixture, with the SW width γ as a unique parameter. We know from previous studies [14,15] that the solid phase of the equimolar mixture is striped, provided that the temperature is low enough. In particular, stripes also appear for very small values of γ , suggesting that their origin is intimately related to the ability of stripe patterns to ensure a higher number of close contacts between unlike particles than possible in configurations with disordered composition. In this paper, we have specifically addressed the role of the mixture concentration χ .

For a moderate concentration asymmetry between the species ($\chi = 0.3$) stripes are still found in the bulk solid phase, at least for sufficiently high density. However, unlike what is observed in the equimolar mixture, novel compositional orders arise when solid and vapor coexist at low temperature: for $\gamma = 1$ the solid droplet has a bcc structure and the minority particles are arranged in a honeycombl-like pattern, while for $\gamma = 0.5$ we observe solid droplets with stripes and square in-plane order of particles.

For a strong concentration asymmetry ($\chi = 0.1$) and $\gamma = 1$ we have seen another type of compositional order in the bulk solid, where minority particles are arranged in a fcc structure with increased spacing. Upon reducing γ to 0.5 , the solid phase becomes compositionally disordered at all temperatures. On the other hand, in the solid-vapor region

for $\gamma = 1$ stripes are present in the solid droplet, whereas for $\gamma = 0.5$ minority particles are arranged in a crystalline structure close to fcc.

To sum up, away from equimolarity the compositional order of the solid droplet is generally different from that of the bulk solid. This occurs because, at low temperature, the droplet adjusts its composition in order to lower the system energy as much as possible. This goal is achieved by making the particle concentration in the droplet closer to equimolarity, which in turn is obtained by expelling majority particles toward the vapor. In all cases, a different compositional order at coexistence is reflected in the behavior of cohesive energy, which at low T is larger in the solid-vapor region than in the bulk solid.

A mixture with the characteristics of our model could be realized by, e.g., DNA-functionalized colloidal particles of two species, as long as the binding affinity between the DNA strands grafted on two unlike particles is reduced by amino-acid substitution [52]. On account of our findings, we expect that even basic colloidal mixtures will exhibit a variety of compositional orders. We hope that the present results will stimulate new experimental efforts and trigger novel applications in photonics and biomedicine.

ACKNOWLEDGMENTS

D.P. acknowledges financial support under the National Recovery and Resilience Plan (NRRP), Mission 4, Component 2, Investment 1.1, Call for Tender No. 104, published on 2.2.2022 by the Italian Ministry of University and Research (MUR), funded by the European Union–NextGenerationEU–Project Title “Thermal Forces in confined fluids and soft solids”–CUP J53D23001310006–Grant Assignment Decree No. 957 adopted on 6.30.2023 by the Italian Ministry of University and Research (MUR). This work has been done using the computer facilities made available by Project No. PO-FESR 2007-2013 MedNETNA (Mediterranean Network for Emerging Nanomaterials).

DATA AVAILABILITY

The data supporting this study’s findings are available from the authors upon reasonable request.

-
- [1] M. Tarzia and A. Coniglio, *Phys. Rev. Lett.* **96**, 075702 (2006).
 - [2] M. Seul and D. Andelman, *Science* **267**, 476 (1995).
 - [3] S. Das, E.-S. M. Duraia, O. D. Velez, M. D. Amiri, and G. W. Beall, *Appl. Surf. Sci.* **435**, 512 (2018).
 - [4] S. C. Glotzer, M. J. Solomon, and N. A. Kotov, *AIChE J.* **50**, 2978 (2004).
 - [5] F. Sciortino and E. Zaccarelli, *Curr. Opin. Solid State Mater. Sci.* **15**, 246 (2011).
 - [6] S. Sacanna, M. Korpics, K. Rodriguez, L. Colon-Mendez, S. H. Kim, and D. J. Pine, *Nat. Commun.* **4**, 1688 (2013).
 - [7] M. Fialkowski, A. Bitner, and B. A. Grzybowski, *Nat. Mater.* **4**, 93 (2005).
 - [8] F. Lo Verso, A. Z. Panagiotopoulos, and C. N. Likos, *Phys. Rev. E* **79**, 010401(R) (2009).
 - [9] S. Watanabe, K. Inukai, S. Mizuta, and M. T. Miyahara, *Langmuir* **25**, 7287 (2009).
 - [10] G. Rosenthal, K. E. Gubbins, and S. H. Klapp, *J. Chem. Phys.* **136**, 174901 (2012).
 - [11] J. J. McManus, P. Charbonneau, E. Zaccarelli, and N. Asherie, *Curr. Opin. Colloid Interface Sci.* **22**, 73 (2016).
 - [12] S. C. Glotzer and M. J. Solomon, *Nat. Mater.* **6**, 557 (2007).
 - [13] D. J. Kraft, R. Ni, F. Smalenburg, M. Hermes, K. Yoon, D. Weitz, A. van Blaaderen, J. Groenewold, M. Dijkstra, and W. Kegel, *Proc. Natl. Acad. Sci. USA* **109**, 10787 (2012).

- [14] G. Munaò, D. Costa, G. Malescio, J. M. Bomont, and S. Prestipino, *Phys. Chem. Chem. Phys.* **25**, 16227 (2023).
- [15] S. Prestipino, D. Pini, D. Costa, G. Malescio, and G. Munaò, *J. Chem. Phys.* **159**, 204902 (2023).
- [16] J. Hou, M. Li, and Y. Song, *Nano Today* **22**, 132 (2018).
- [17] H. Mohwald, *Thin Solid Films* **159**, 1 (1988).
- [18] S. L. Keller and H. M. McConnell, *Phys. Rev. Lett.* **82**, 1602 (1999).
- [19] P. Akcora *et al.*, *Nat. Mater.* **8**, 354 (2009).
- [20] G. Malescio and G. Pellicane, *Nat. Mater.* **2**, 97 (2003).
- [21] G. Malescio and G. Pellicane, *Phys. Rev. E* **70**, 021202 (2004).
- [22] H. Pattabhiraman and M. Dijkstra, *Soft Matter* **13**, 4418 (2017).
- [23] Y. D. Fomin, E. N. Tsiok, and V. N. Ryzhov, *Phys. A (Amsterdam)* **527**, 121401 (2019).
- [24] G. Costa and S. Prestipino, *Entropy* **27**, 46 (2025).
- [25] J. Pękański, A. Ciach, and N. G. Almarza, *J. Chem. Phys.* **140**, 114701 (2014).
- [26] N. G. Almarza, J. Pękański, and A. Ciach, *J. Chem. Phys.* **140**, 164708 (2014).
- [27] D. McDermott, C. J. O. Reichhardt, and C. Reichhardt, *Soft Matter* **10**, 6332 (2014).
- [28] D. Pini and A. Parola, *Soft Matter* **13**, 9259 (2017).
- [29] D. Pini, *Soft Matter* **14**, 6595 (2018).
- [30] A. De Virgiliis, A. Meyra, and A. Ciach, *Molecules* **29**, 1512 (2024).
- [31] C. I. Mendoza and E. Batta, *Europhys. Lett.* **85**, 56004 (2009).
- [32] A. Ciach, *Mol. Phys.* **109**, 1101 (2011).
- [33] A. Ciach, A. De Virgiliis, A. Meyra, and M. Litniewski, *Molecules* **28**, 1366 (2023).
- [34] O. Patsahan, A. Meyra, and A. Ciach, *Soft Matter* **20**, 1410 (2024).
- [35] L. A. Padilla, A. A. León-Islas, J. Funkhouser, J. C. Armas-Pérez, and A. Ramírez-Hernández, *J. Chem. Phys.* **155**, 214901 (2021).
- [36] G. Munaò, D. Costa, G. Malescio, J. M. Bomont, and S. Prestipino, *Soft Matter* **18**, 6453 (2022).
- [37] A. De Virgiliis, A. Meyra, and A. Ciach, *Curr. Issues Mol. Biol.* **46**, 10829 (2024).
- [38] H. J. Zhao, V. R. Misko, and F. M. Peeters, *New J. Phys.* **14**, 063032 (2012).
- [39] C. Bores, E. Lomba, A. Perera, and N. G. Almarza, *J. Chem. Phys.* **143**, 084501 (2015).
- [40] P. J. in 't Veld, S. J. Plimpton, and G. S. Grest, *Comput. Phys. Commun.* **179**, 320 (2008).
- [41] G. Munaò, S. Prestipino, J. M. Bomont, and D. Costa, *J. Phys. Chem. B* **126**, 2027 (2022).
- [42] G. Munaò, D. Costa, S. Prestipino, and C. Caccamo, *Phys. Chem. Chem. Phys.* **18**, 24922 (2016).
- [43] A. Patti and A. Cuetos, *Mol. Simul.* **44**, 516 (2018).
- [44] D. Frenkel and B. Smit, *Understanding Molecular Simulations*, 2nd ed. (Academic Press, New York, 2002).
- [45] P. J. Steinhardt, D. R. Nelson, and M. Ronchetti, *Phys. Rev. B* **28**, 784 (1983).
- [46] P. R. ten Wolde, M. J. Ruiz-Montero, and D. Frenkel, *J. Chem. Phys.* **104**, 9932 (1996).
- [47] S. Prestipino, *J. Chem. Phys.* **148**, 124505 (2018).
- [48] D. Pini, S. Prestipino, D. Costa, G. Malescio, and G. Munaò (unpublished).
- [49] K. Binder, P. Virnau, B. J. Block, P. Virnau, and A. Tröster, *Am. J. Phys.* **80**, 1099 (2012).
- [50] S. Prestipino, C. Caccamo, D. Costa, G. Malescio, and G. Munaò, *Phys. Rev. E* **92**, 022141 (2015).
- [51] M. C. Abramo, C. Caccamo, D. Costa, P. V. Giaquinta, G. Malescio, G. Munaò, and S. Prestipino, *J. Chem. Phys.* **142**, 214502 (2015).
- [52] T. Sunami and H. Kono, *Protein Sci.* **28**, 1630 (2019).